Journal of MATERIALS RESEARCH

Article
DOI:10.1557/s43578-022-00543-z

Microstructure evolution, crystallography, nanomechanical properties and wear-resistance of multi-component M_2B in Fe–B alloy

Suocheng Song[1], Yanliang Yi[2,3,a], Jiandong Xing[4], Hanguang Fu[5]

[1] Center for Alloy Innovation and Design, State Key Laboratory for Mechanical Behavior of Materials, Xi'an Jiaotong University, Xi'an 710049, China
[2] Institute of Advance Wear & Corrosion Resistant and Functional Materials, Jinan University, Guangzhou 510632, Guangdong, People's Republic of China
[3] Shaoguan Research Institute of Jinan University, 168 Muxi Avenue, Shaoguan 512027, China
[4] State Key Laboratory for Mechanical Behavior of Materials, School of Materials Science and Engineering, Xi'an Jiaotong University, No. 28, Xianning West Road, Xi'an 710049, Shaanxi Province, People's Republic of China
[5] Research Institute of Advanced Materials Processing Technology, School of Materials Science and Engineering, Beijing University of Technology, Beijing 100124, People's Republic of China
[a] Address all correspondence to this author. e-mail: y_yanliang@163.com

Received: 17 November 2021; accepted: 16 March 2022; published online: 18 April 2022

To investigate the basic characteristics of multi-component boride in Fe–B alloy, the samples were prepared by directional solidification, and then the microstructural evolution, crystallography, nanomechanical properties and wear-resistance of multi-component M_2B have been systematically studied. The results show that the boride grows in the sequence of Mo-rich → Fe-rich → Cr-rich M_2B. The Mo-rich M_2B has the body centered tetragonal (bct) structure with stoichiometry of $Fe_{0.72}Cr_{0.27}Mo_{0.80}(B,C)$, the Fe-rich M_2B possesses the bct structure with stoichiometry of $Fe_{1.59}Cr_{0.38}Mo_{0.08}(B,C)$, while the Cr-rich M_2B owns the body centered orthorhombic (bco) structure with stoichiometry of $Fe_{1.48}Cr_{0.50}Mo_{0.02}(B,C)$. Moreover, the Mo addition can facilitate more dislocations in the M_2B compared to the Cr addition. Thus, the Mo-rich M_2B has the best stiffness and toughness, followed by the Cr-rich M_2B and then the Fe-rich M_2B. Additionally, the Mo-rich and Cr-rich M_2B can possess higher wear-resistance relative to the Fe-rich M_2B.

Introduction

Nowadays, considerable amounts of energy consumption and economic loss are caused by the friction and wear in industrial equipment, thus it's imperative to design environmentally and energy-saving wear-resistant materials [1–3]. Until now, iron-based wear-resistant material containing certain B and C contents was widely applied, because of the existence of intermetallic compounds (e.g., Fe_2B [2], Cr_7C_3 [3] or Fe_3C [4]). Compared to the Cr_7C_3 or Fe_3C, the Fe_2B has higher hardness and heat stability, thus leading to better wear-resistance [5, 6]. As boron is difficult to dissolve into iron, it mainly segregates at grain boundaries to form Fe_2B [7–9]. Therefore, Fe–B alloy can be designed on the basis of the fundamental concept of replacing the carbide in iron with Fe_2B.

Thus far, Fe–B alloy has attracted more and more attention as a novel wear-resistant material. Ren et al. [10] reported that increasing B content could increase the volume of Fe_2B, which effectively improved the wear-resistance of Fe–B alloy. Zhang et al. [11] revealed the effect of hot forging on the mechanical properties and wear-resistance of Fe–B alloy. The results showed that the toughness and wear-resistance of alloy increased considerably after hot forging. Yi et al. [12] optimized the cooling rate for designing Fe–B alloy with high-performance. The effect of cooling rate on microstructure, mechanical properties and residual stress of Fe–B alloy was investigated. Results showed that the critical cooling rate of martensite transformation may be optimal quenching rate of alloy. Yi et al. [6] has also discussed the effect of matrix microstructure on the abrasive wear behavior of Fe–B alloy. It had been proven that the Fe–B alloy with high V_m/V_p (where the V_m/V_p indicates the volume ratio of martensite to pearlite) could effectively subject to severe abrasive wear in a low contact stress. As a new wear-resistant material,

Fe–B alloy has been put into production, and achieved very good economic benefits. Scholars have developed Fe–B alloy-based rolls, mud pump impeller blades and glass molds [13, 14]. Such as, the service life of Fe–B alloy-based roller is about 8 times than that of ductile iron-based roller.

As mentioned above, Fe–B alloy can possess excellent wear-resistance, which is mainly related to the existence of Fe_2B. During the wear process of Fe–B alloy, the Fe_2B resists abrasive and protects metallic matrix from being shoveled off. However, the Fe_2B possesses inherent brittleness because of the weak B–B bond in [002] direction [15, 16]. This will decrease the wear-resistance of Fe–B alloy due to a great susceptibility to cracking. That is, it is particularly necessary to toughen the Fe_2B. Jian et al. [17] indicated that transition metal element Cr could replace partial Fe atom in Fe_2B crystal, which could improve the toughness of M_2B-type (M = Cr, Fe and Mo) boride, improving the wear-resistance of Fe–B alloy as a result. Similarly, Yi et al. [18] revealed that Mo addition could also form multi-component M_2B in Fe–B alloy. Except for these, Xiao et al. [19–21] investigated the fundamental properties of M_2B so as to provide a guidance for its real application. And the values of bulk modulus for Cr_2B, Fe_2B and Mo_2B were 279.56, 249.73 and 289.43 GPa, respectively.

To sum up, the formation of multi-component M_2B is significant for the wear-resistance of Fe–B alloy. Thus, it is imperative to study the basic characteristics of various multi-component M_2B in the Fe–B alloy. However, few investigations on the microstructure evolution, crystallography, nanomechanical properties, and wear-resistance of multi-component M_2B in Fe–B alloy have been reported. In this work, the microstructure evolution of multi-component M_2B in Fe–B alloy is systematically analyzed using directional solidification method (DS). Accordingly, the crystallography, nanomechanical properties and wear-resistance of multi-component M_2B were discussed in detail. Even more, the study aims to make contributions to further design of Fe–B alloy with high-performance.

Result and discussion

Microstructure evolution

Figure 1 shows phase diagram of the tested alloy during equilibrium solidification process. When the solidification temperature drops to 1316 °C (point 3), the δ-Fe precipitates from liquid melt firstly, owing to the transformation of L → δ-Fe. This is because the tested alloy has high content of ferrite stabilizer elements (Mo, Cr, Al, V), which leads to the formation of δ-Fe as

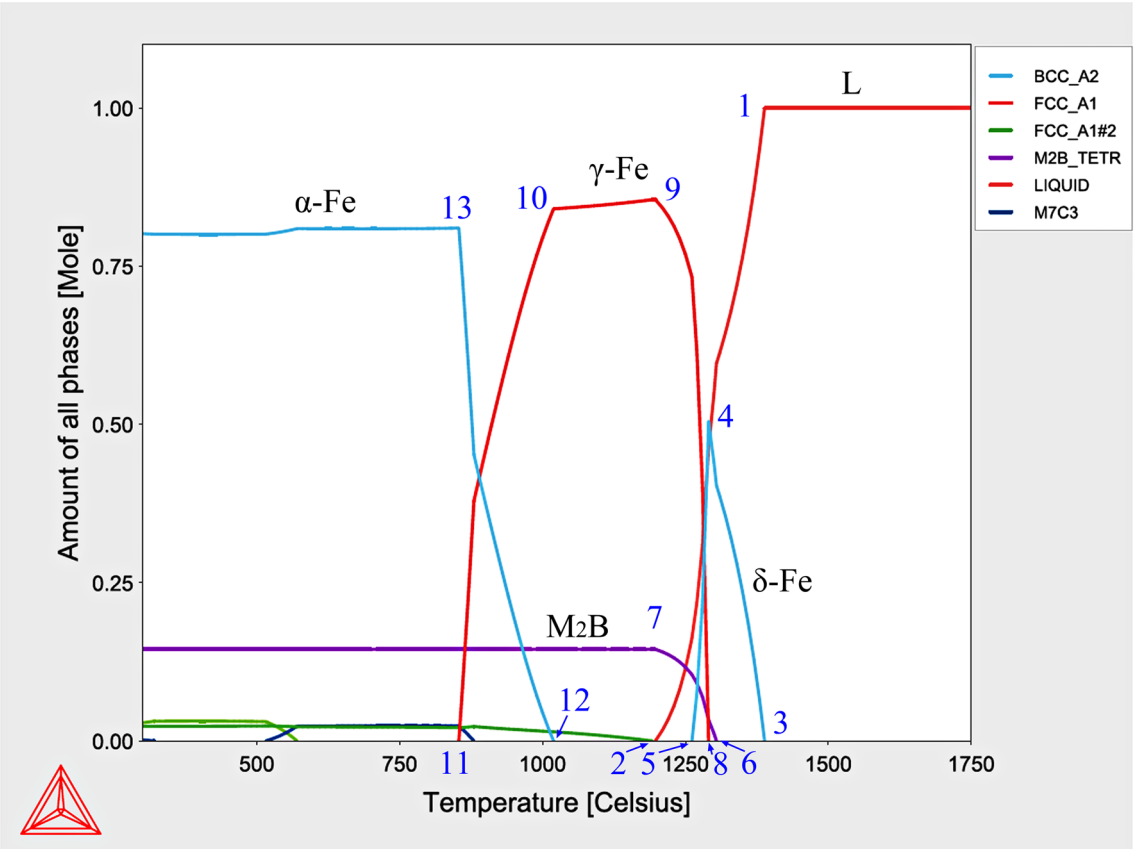

Figure 1: Thermo-calc calculation of the tested Fe–B alloy.

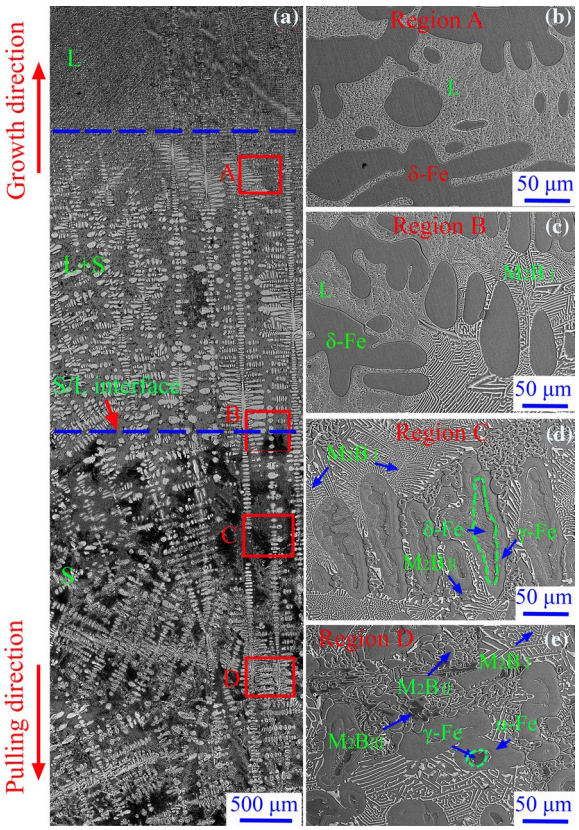

Figure 2: Macro- and micro-structures of the tested DS bar: (a) Longitudinal-section macrostructure; (b)–(e) Microstructures of the A, B, C and D regions.

primary phase [22, 23]. As the solidification temperature drops from 1213 °C (point 6) to 1081 °C (point 7), the alloying elements (e.g., Cr, Mo, V or B) are remained in residual liquid melt accompanied with the growth of δ-Fe [24–26]. As a result, the transformations of L + δ-Fe → γ-Fe and L → γ-Fe + M_2B occur, just as reported in previous researches [25–28]. With the further decrease of solidification temperature (point 12 → point 13), pearlitic transformation occurs, and then the γ-Fe is converted to α-Fe at 869 °C.

Figure 2 shows the macro- and micro-structures of the studied DS bar. From the macrostructures, the DS bar can be divided into three parts [Fig. 2(a)]. The upper part is "liquid region (L)" caused by sudden power termination, the bottom part is "stable solidification region (S)", and the middle part is "mushy zone (S + L)". The relatively well-aligned grains grow along external coordinate *c*-axis. From the microstructures, the dendritic δ phase forms in liquid melt firstly [Fig. 2(b)]. As solidification temperature drops, the M_2B forms subsequently because of the transformation of L → γ-Fe + M_2B. Herein, the white-coralloid M_2B_I forms firstly [Fig. 2(c)], the light-coloured rod-like M_2B_{II} acts as following phase [Fig. 2(d)], and then the dark-coloured blocky M_2B_{III} appears [Fig. 2(e)]. Meanwhile, the metallic matrix changes from δ-Fe to γ-Fe and then to α-Fe with the decrease of solidification temperature. The experimental results are in agreement with the calculated phase diagram.

To clarify alloying element distribution in the multi-component M_2B, the corresponding composition is examined using EPMA, as listed in Table 1. The stoichiometry of M_2B is calculated by the formula of $M_x(B,C)_y$. The *x* and *y* represent (Fe, Mo, Cr, etc.) at% and (B,C) at%, respectively. From Table 1, the M_2B_I is rich in Mo, and the stoichiometry is $Fe_{0.72}Cr_{0.27}Mo_{0.80}(B,C)$, closing to the $M_{1.96}B$-type boride [7–9, 29, 30]. The M_2B_{II} is rich in Fe, and the stoichiometry is $Fe_{1.59}Cr_{0.38}Mo_{0.08}(B,C)$, which tends to be the $M_{2.09}B$ [7–9, 30, 39]. However, the M_2B_{III} is rich in Cr and deficient in Mo, possessing a stoichiometry of $Fe_{1.48}Cr_{0.50}Mo_{0.02}(B,C)$, closing to the $M_{2.03}B$ [7–9, 30, 39]. According to the element periodic table, the atomic radius R_{Cr}, R_{Mo} and R_{Fe} are 0.185, 0.201 and 0.172 nm, respectively, and the electronegativity X_p^{Cr}, X_p^{Fe} and X_p^{Mo} are 1.66, 1.83 and 2.16, respectively. Therefore, the similar electronegativity and atomic radius result in that Mo or Cr atom can replace Fe atom in Fe_2B crystal. Combined with the microstructures, it can be known that the multi-component M_2B forms in a sequence of Mo-rich → Fe-rich → Cr-rich M_2B. This may be because the Gibbs free energies of various M_2B (M = Mo, Cr or Fe) are $G_{Mo2B} < G_{Fe2B} < G_{Cr2B}$ [17–19]. Another factor identified in this work is the partition coefficient of alloying element, such as the partition coefficients are 0.51 and 0.34 for the Mo and Cr atoms, respectively [31].

Crystal structure analysis

Figure 3 shows bright-field TEM micrographs and corresponding selected area diffraction patterns (SADPs) of the multi-component M_2B. From Fig. 3(a) and d, it can be observed that the rod-like Fe-rich M_2B is a bct structure with the lattice parameter of $a = b = 0.5109$ nm, $c = 0.4249$ nm and $c/a = 0.83$ (C16, $CuAl_2$-type structure). From Fig. 3(b) and e, the coralloid-like Mo-rich M_2B is clearly distinguished and indexed to a bct structure ($a = b = 0.5547$ nm, $c = 0.4739$ nm and $c/a = 0.85$). From Fig. 3(c) and (f), the blocky Cr-rich M_2B has a bco structure with lattice parameter of $a = 1.4583$ nm, $b = 0.7379$ nm and $c = 0.4245$ nm. Moreover, compared with the Fe_2B-rich M_2B, the lattice constants of Cr-rich and Mo-rich M_2B have an obvious increase. These mean that the addition of alloying elements Cr and Mo can affect the crystal structure of Fe_2B. Except for these, Ma et al. [7–9] revealed that a possible orientation relationship (OR) between bco M_2B and metallic matrix was $\langle 1\text{–}10\rangle_{M2B}//\langle 110\rangle_{\alpha}$, while a possible OR between bct M_2B and metallic matrix was $\langle 002\rangle_{M2B}//\langle 110\rangle_{\alpha}$. Similarly, a possible OR between bct M_2B and metallic matrix detected by electron back-scattering diffraction was $\langle 001\rangle_{M2B}//\langle 001\rangle_{\alpha}$ [29].

TABLE 1: Electron microprobe analysis of the multi-component M_2B in Fe–B alloy.

M_2B	Element (at%)							Calculated formula	
	B	C	Cr	Mn	Fe	V	Mo		
Mo-rich M_2B	21.97	10.11	12.00	0.66	51.17	1.31	2.78	$Fe_{1.59}Cr_{0.38}V_{0.04}Mo_{0.08}(B,C)$	$\sim M_{1.96}B$
Cr-rich M_2B	30.03	2.72	16.43	0.59	48.49	0.99	0.75	$Fe_{1.48}Cr_{0.50}V_{0.03}Mo_{0.02}(B,C)$	$\sim M_{2.03}B$
Fe-rich M_2B	31.86	4.81	6.23	0.33	24.06	5.76	26.95	$Fe_{0.72}Cr_{0.27}V_{0.17}Mo_{0.80}(B,C)$	$\sim M_{2.09}B$

In order to investigate the detailed substructure of multi-component M_2B, the high-resolution transmission electron microscope (HRTEM) and corresponding fourier-filtered transform (FFT) images are detected as shown in Fig. 4. From Fig. 4(a), the interplanar distance of the (404) plane for the Fe-rich M_2B is 0.612 nm, and nearly no obvious defects can be observed. From Fig. 4(b), the interplanar distance of the (002) plane for the Cr-rich M_2B is 0.235 nm, and several defects can be found in the M_2B. To be exact, the Burgers vector is marked by drawing a frame enclosing non-perfect zone. Two extra half-planes are inserted from the bottom and right sides of Burgers frame. This represents two full dislocations with Burgers. Moreover, the central area enclosed with circle can be indexed to an edge dislocation, which is marked by the "T". From Fig. 4(c), more edge dislocations can be found in the Mo-rich M_2B. Several stacking faults can be found in the region A, and spatial distribution of dislocations can be observed in the region B. This reveals that the addition of Cr and Mo facilitates the formation of dislocation in the M_2B. Compared to the Cr addition, the Mo addition can induce the formation of more dislocations. Just as reported in previous works [17, 18], the Mo or Cr addition can affect the electron environment of B-B bond, which changes the density of surrounding B electrons, leading to the formation of dislocation in Fe_2B crystal as a result.

Nanomechanical properties

Figure 5 shows the *P*–*h* curves of multi-component M_2B in the tested DS sample at the load of 1×10^{-2} N using nanoindentation. It can be found that pop-ins occur in the *P*–*h* curves. And they occur in the Fe-rich, Cr-rich and Mo-rich M_2B when the load reaches 4.62×10^{-2}, 6.11×10^{-2} and 8.66×10^{-2} N, respectively. Moreover, the hardness (*H*) and Young's modulus (*E*) of M_2B are calculated according to the Oliver-Pharr method. The results are listed in Table 2. It can be known that, the *H* values of Fe-rich, Cr-rich and Mo-rich M_2B are 18.82, 21.22 and 24.86 GPa, respectively, and the *E* values of Fe-rich, Cr-rich and Mo-rich M_2B are 203.85, 225.77 and 255.57 GPa, respectively. The Mo-rich M_2B exhibits the best stiffness, followed by the Cr-rich M_2B and then the Fe-rich M_2B. Except for these, the "plasticity factor, δ_A" for quantifying the brittleness of M_2B are calculated. The δ_A of Fe-rich, Cr-rich and Mo-rich M_2B is 0.25, 0.29 and 0.32, respectively. Compared to the Fe-rich M_2B, the Mo-rich and Cr-rich M_2B possess better toughness. As previous reports discussed, pure Fe_2B belongs to the bcc structure

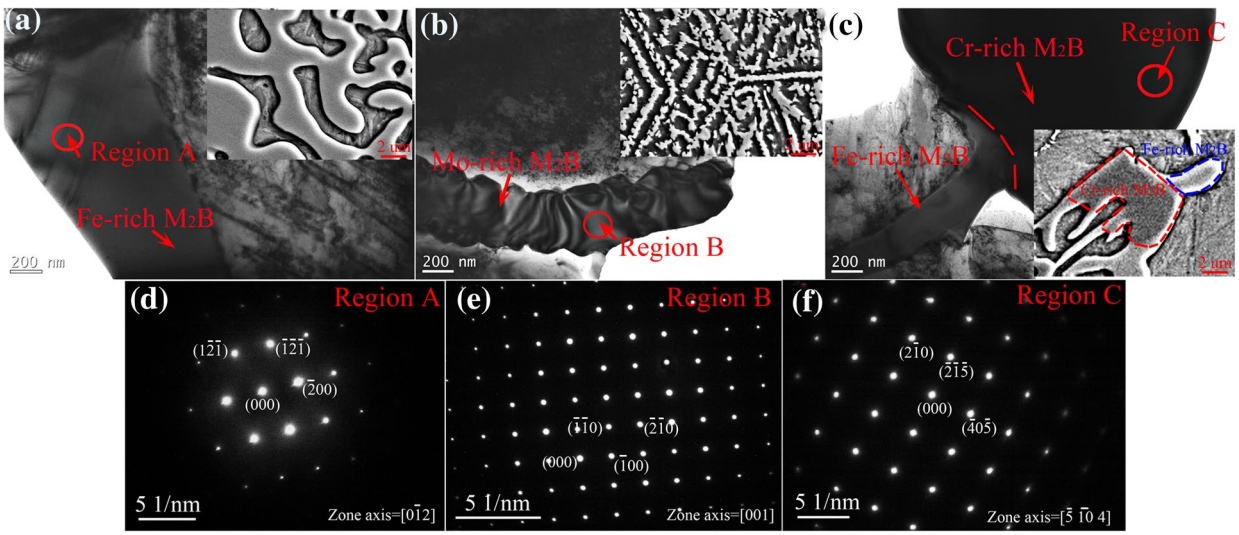

Figure 3: Bright-field TEM micrographs and corresponding selected area diffraction patterns (SADPs) of the multi-component M_2B in Fe–B alloy: (a), (b) and (c) show TEM micrographs of the Fe-rich, Mo-rich and Cr-rich M_2B, respectively; (d), (e) and (f) show corresponding SADPs of the Fe-rich, Mo-rich and Cr-rich M_2B, respectively.

(C16, CuAl2-type) and space group of I4/mcm (No. 140) [7–9, 19–21]. With the addition of alloying elements (Cr and Mo), the bcc Fe_2B changes to the bct or bco M_2B. This may affect the electron environment of B–B bond. As the B–B bond in M_2B crystal is weak in [002] direction, the change of electron environment may strengthen the B–B bond, thus the δ_A value of M_2B increase as a result. Furthermore, the formation of dislocation may also facilitate the improvement of H and E values in the M_2B. Just as shown in the reference [32], the formation of dislocation improved the strength of M_7C_3-type carbide owing

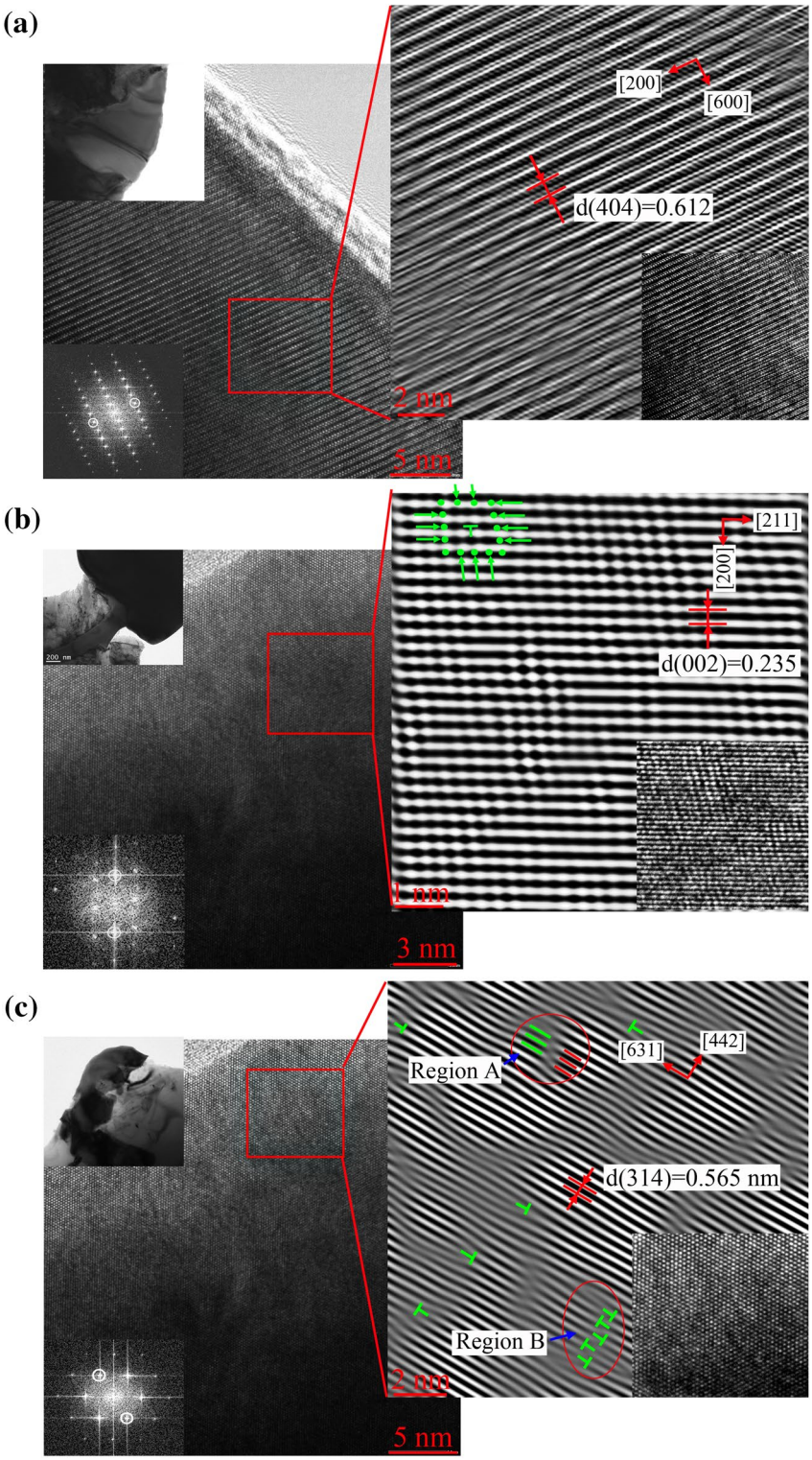

Figure 4: High-resolution transmission electron microscopy (HRTEM) images and Fourier-filtered transform (FFT) images of the multi-component M_2B: (a) Fe-rich M_2B; (b) Cr-rich M_2B;(c) Mo-rich M_2B.

to the increase of sub-grain boundaries. To some extent, the result reveals that the addition of Cr or Mo can improve the hardness and toughness of multi-component M_2B.

Wear-resistance

Recently, nanoindentation was applied to evaluate wear-resistance of material [33–35]. In fact, the wear-resistance of material refers to its elastic strain, which can be calculated by the ratio of H/E [34]. Additionally, another parameter (H^3/E^2) relating to yield pressure reflects the resistance to plastic deformation, which can also assess the wear-resistance of material [35]. In this work, the H/E and H^3/E^2 of multi-component M_2B are calculated as shown in Table 3. Visibly, the Mo-rich M_2B has the largest H/E and H^3/E^2, followed by the Cr-rich M_2B and then the Fe-rich M_2B. To some extent, it indicates that the addition of Mo or Cr can improve the wear-resistance of multi-component M_2B.

To further verify above mentioned deduction, the worn morphologies of multi-component M_2B at different loads are observed using SEM, as shown in Fig. 6. When the normal load is 7 N [Fig. 6(a)], the Fe-rich and Mo-rich M_2B are shallowly scraped off, and there are nearly no obvious microcracks existing in the M_2B. As the normal load increases to 9 N [Fig. 6(b)], the Fe-rich M_2B occurs fracture, while the Mo-rich M_2B is lightly scratched. With the increase of normal load to 15 N [Fig. 6(c)], the Mo-rich and Fe-rich M_2B has been damaged, while the Mo-rich M_2B possesses higher wear-resistance

TABLE 2: Nanoindentation results (hardness, Young's modulus and plasticity factor) for the multi-component M_2B of Fe–B alloy at the load of 1×10^{-2} N for 5 s.

Multi-component M_2B	H (GPa)	E (GPa)	δ_A
Fe-rich M_2B	18.82	203.85	0.25
Cr-rich M_2B	21.22	225.77	0.29
Mo-rich M_2B	24.86	255.57	0.32

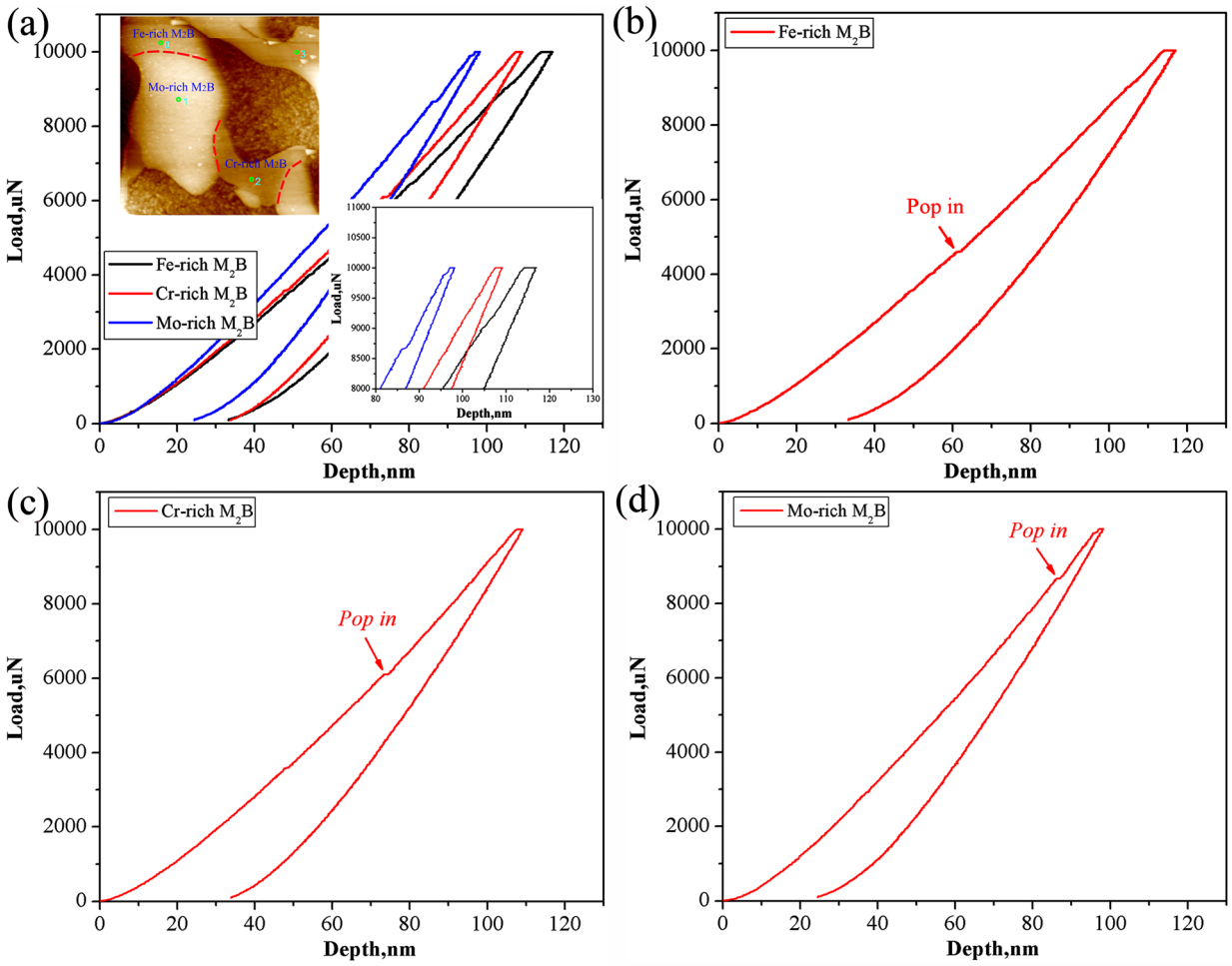

Figure 5: *P–h* curves of the multi-component M_2B in Fe–B alloy through nanoindentation at the load of 1×10^{-2} N for 5 s.

relative to the Fe-rich M_2B. According to previous works [6, 10], the M_2B resists the abrasives and protects material from being shoveled off during the wear process of Fe–B alloy. If the H/E and H^3/E^2 of M_2B is low (e.g., Fe-rich M_2B), the brittle M_2B can't resist the abrasives, as a result the M_2B tends to fracture easily. With higher H/E and H^3/E^2, the initiation of microcracks can be inhibited in the M_2B, owing to higher resistance to plastic deformation. Thus, the undamaged M_2B can resist the abrasive better.

Conclusions

The multi-component M_2B is significant for the wear-resistance of Fe–B alloy. To study the basic characteristics of multi-component M_2B, the Fe–B alloy has been prepared using directional solidification, and then the microstructural evolution, crystallography, nanomechanical properties and wear-resistance of multi-component M_2B have been systematically investigated. The main conclusions are as follows:

(1) During the solidification process, the multi-component M_2B of Fe–B alloy grows in the sequence of Mo-rich → Fe-rich → Cr-rich M_2B. The Mo-rich M_2B possesses white-coralloid structure, the Fe-rich M_2B has light-coloured rod-like structure, and the Cr-rich M_2B shows dark-coloured blocky structure.

(2) In the Fe–B alloy, the Fe-rich M_2B has a stoichiometry of $Fe_{1.59}Cr_{0.38}Mo_{0.08}(B, C)$ with the bct structure ($a = b = 0.5109$ nm, $c = 0.4249$ nm and $c/a = 0.83$), the Mo-rich M_2B possesses a stoichiometry of $Fe_{0.72}Cr_{0.27}Mo_{0.80}(B, C)$ with the bct structure ($a = b = 0.5547$ nm, $c = 0.4739$ nm and $c/a = 0.85$), while the Cr-rich M_2B owns a stoichiometry of $Fe_{1.48}Cr_{0.50}Mo_{0.02}(B, C)$ with the bco structure ($a = 1.4583$ nm, $b = 0.7379$ nm and $c = 0.4245$ nm).

(3) The addition of Cr or Mo leads to the formation of dislocation in multi-component M_2B, and the Mo addition can induce more dislocations relative to the Cr addition. This Cr/Mo addition facilitates the hardness and toughness of Fe_2B. The hardness H of Fe-rich, Cr-rich and Mo-rich M_2B is 18.82, 21.22 and 24.86 GPa, respectively, and the plasticity factor δ_A of Fe-rich, Cr-rich and Mo-rich M_2B is 0.25, 0.29 and 0.32, respectively.

(4) With the higher hardness and toughness, the initiation of microcracks can be inhibited in the M_2B owing to higher resistance to plastic deformation, thus the Mo-rich and Cr-rich M_2B possess higher wear-resistance relative to the Fe-rich M_2B.

TABLE 3: H/E and H^3/E^2 of the multi-component M_2B in Fe–B alloy.

Multi-component M_2B	H/E ($\times 10^{-2}$)	H^3/E^2 (GPa $\times 10^{-1}$)
Fe-rich M_2B	9.23	1.60
Cr-rich M_2B	9.40	1.87
Mo-rich M_2B	9.73	2.35

Experimental procedures

Directional solidification

The directional solidification has been widely applied to analyze microstructure evolution or growth mechanism of alloy [36–38]. In the present work, a Y-type block ingot was prepared using vacuum induction furnace, depending on a nominal chemical composition. Subsequently, some $\phi 4$ mm × 10 mm bars were spark cut from the ingot. The directional solidification test was performed on a Bridgman-type directional furnace. The prepared bars were firstly loaded into an alumina tube crucible with inner diameter of 8 mm and length of 150 mm, followed by putting into induction furnace column, and then heated up to 1600 °C for 10 min. Finally, the tube crucible was quenched into cooling liquid with the withdrawal rate of 15 um/s for 20 min. The schematic of directional solidification and corresponding mushy zone is shown in Fig. 7. The final composition of sample was measured by X-ray fluorescence spectrometer (S8 TIGER), the result was listed as follows (wt%): B 1.80, C 0.41, Cr 5.36, Mo 8.34, Al 0.71, Si 1.03, V 0.97, Mn 0.62 and Fe in balance.

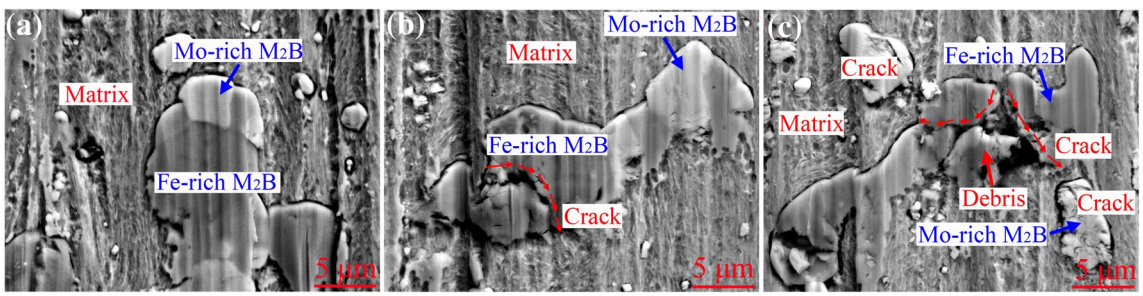

Figure 6: Worn morphologies of the multi-component M_2B in Fe–B alloy at the loads of 7 ~ 15 N, using SiC as abrasive: (a) 7 N; (b) 9 N; (c) 15 N.

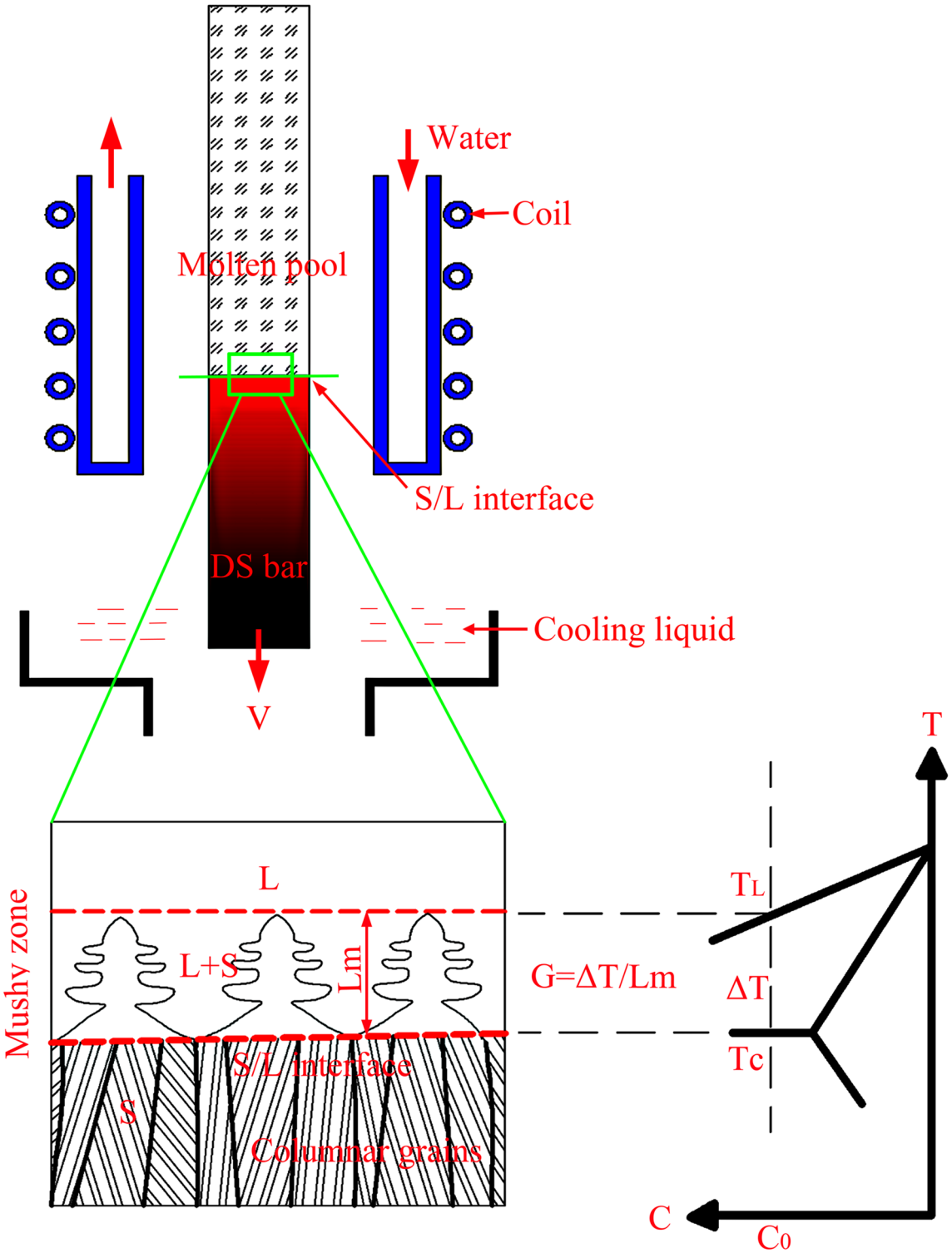

Figure 7: Schematic of directional solidification and corresponding mushy zone.

Characterization and phase diagram calculation

After wire-cutting, grinding and polishing, the DS sample was etched with 4 vol% nital solution for metallographic characterization. Subsequently, the etched DS sample was observed by light microscopy (OM, LEICA DMI 5000M) and scanning electron microscope (SEM, JSM-7000F). To measure alloying element distribution, electron probe microanalysis (EPMA, JXA-8230) equipped with wavelength dispersive X-ray (WDX) was applied. The EPMA measurement was scanned at 10 keV and 100 nA with the scanning range of 40–75 Å and step size of 0.01 Å. High-resolution transmission electron microscope (HRTEM, JEM-F200) was used to analyze the crystallography of multi-component M_2B. Thin foils with the thickness of 0.5 mm for transmission electron microscope observation were prepared using spark erosion machine. Subsequently, they were mechanically ground by hand to about 50 um, followed by punching out some discs of 3 mm in diameter. The thin discs were twin-jet electropolished to electron transparency at 75% methanol, 5% perchloric acid and 20% glycerol maintained at 0 °C. Some thin foils were then thinned to about 30 um for HRTEM observation, which was operated at 400 keV with an incidence angle of 4° for 30 min. The high-resolution images were gathered at a point-to-point resolution of ~ 1.7 Å, and analyzed subsequently using Digital Micrograph software.

Thermo-Calc calculation software, containing a sophisticated database (thermo-chemical databank) and programming interface package, is often utilized to calculate the equilibrium phase diagram [39]. In this work, the POLY-3 calculation (a type of calculation in Thermo-Calc software with TCFE-7 database.) was chosen. The selected parameters mainly included the temperature range of 500–1750 °C and the pressure of 150 kPa. Calculated criterion was the minimization of Gibbs free energy.

Nanoindentation

The metallographic sample was prepared for nanoindentation on the UMIS instrument and triboindenter (from Hysitron Inc.) at 1×10^{-2} N load for 5 s, following the ASTM E2546. The displacement (depth) of indenter was continuously monitored so as to record the load–displacement (P–h) curve. All measurements were performed in air currents.

The hardness (H) and Young's modulus (E) of multi-component M_2B were calculated using the Oliver–Pharr method via the Eqs. 1–4 [40].

$$H = \frac{P_{\max}}{Ah_c} \tag{1}$$

where P_{max} is the maximum load, A is the contact area between material and indenter at the load of P_{max}, and h_c is the depth. The h_c was calculated by the Eq. 2.

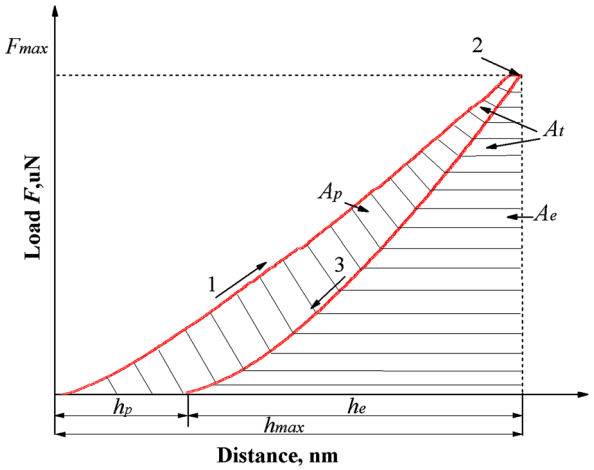

Figure 8: Schematic of the P–h curve for Berkovich indenter: (1) Loading curve; (2) Holding curve at the P_{max}; (3) Unloading curve.

$$hc = h_{\max} - \varepsilon \frac{P_{\max}}{S} \tag{2}$$

where ε is 0.75 for the Berkovich indenter, S is the initial unloading stiffness at the load of P_{max}.

The E could be reduced by the Eqs. 3 and 4.

$$\frac{1}{E_{\text{eff}}} = \frac{(1-\nu^2)}{E} + \frac{(1-\nu_i^2)}{E_i} \tag{3}$$

$$E_{\text{eff}} = \frac{1}{\beta}\frac{\sqrt{\pi}}{2}\frac{S}{\sqrt{A}} \tag{4}$$

where E_i is the modulus of indenter, and ν and ν_i are Poisson's ratio of material and indenter, respectively. E_{eff} is the effective elastic modulus. β is 1.034 for the Berkovich indenter.

Additionally, the plasticity characteristic of multi-component M_2B (plasticity factor, δ_A) was calculated by the Eq. 5 [41].

$$\delta_A = \frac{A_p}{A_t} = 1 - \frac{A_e}{A_t} \tag{5}$$

where A_e and A_t are the areas under the unloading and loading curves, respectively ($A_p = A_t - A_e$), as shown in Fig. 8.

Abrasive wear behavior

Wear tests were carried out on a ML-100 type pin-on-disk apparatus with pin sample against SiC abrasive paper (240 mesh/60 um, 2600 HV [17, 18]). The pin samples with the size of ϕ6 mm × 10 mm were spark cut from the DS sample. The tests were performed in a spiral track with main parameters of sliding distance of 6 m, rotating rate of 60 $r{\cdot}\text{min}^{-1}$, sliding rate of 4 $\text{mm}{\cdot}r^{-1}$ and normal loads of 7–15 N.

Acknowledgments

This work was financially supported by National Natural Science Foundation of China (No. 52005217), Basic and Applied Basic Research Fund Project of Guangdong Province in China (No. 2021A1515010523 and No. 2020A1515110020) and Basic Scientific Research Projects of Central Universities (No. 21620344).

Data availability

The datasets generated during and/or analyzed during the current study are available from the corresponding author on reasonable request.

Declarations

Conflict of interest There are no conflicts to declare.

References

1. P. Xiao, Y.M. Gao, C.C. Yang, Z.W. Liu, Y.F. Li, F.X. Xu, Microstructure, mechanical properties and strengthening mechanisms of Mg matrix composites reinforced with in situ nanosized TiB2 particles. Mater. Sci. Eng. A **710**, 251–259 (2018)
2. Z.F. Huang, S.Q. Ma, J.D. Xing, B.Y. Wang, Bulk Fe_2B crystal fabricated by mechanical ball milling and plasma activated sintering. J. Alloy. Compd. **582**, 196–200 (2014)
3. G.B. Ying, X.D. He, M.W. Li, S.Y. Du, W.B. Han, F. He, Effect of Cr_7C_3 on the mechanical, thermal, and electrical properties of Cr_2AlC. J. Alloy. Comp. **509**, 8022–8027 (2011)
4. Y. Mitsui, Y. Ikehara, K. Takahashi, S. Kimura, G. Miyamoto, T. Furuhara, K. Watanabe, K. Koyama, Fe-Fe_3C binary phase diagram in high magnetic fields. J. Alloy. Compd. **632**, 251–255 (2015)
5. Z. Lv, H.G. Fu, J.D. Xing, Z.F. Huang, S.Q. Ma, Y. Hu, Influence of boron contents on oxidation behavior and the diffusion mechanism of Fe–B based alloys at 1073K in air. Corros. Sci. **108**, 185–193 (2016)
6. Y.L. Yi, J.D. Xing, Y.F. Lu, Y.M. Gao, H.G. Fu, L.L. Yu, M.J. Wan, Q.L. Zheng, Effect of normal load on two-body abrasive wear of an Fe-B-Cr-C based alloy with minor Cu and Ni additions. Wear **408**, 160–170 (2018)
7. S.Q. Ma, J.D. Xing, H.G. Fu, Y.L. He, Y. Bai, Y.F. Li, Y.P. Bai, Interface characteristics and corrosion behaviour of oriented bulk Fe_2B alloy in liquid zinc. Corros. Sci. **78**, 71–80 (2014)
8. S.Q. Ma, J.D. Xing, H.G. Fu, Y.M. Gao, J.J. Zhang, Microstructure and crystallography of borides and secondary precipitation in 18 wt.% Cr–4 wt.% Ni–1 wt.% Mo–3.5 wt.% B–0.27 wt.% C steel. Acta. Mater. **60**, 831–843 (2012)
9. S.Q. Ma, J.D. Xing, Y.L. He, H.G. Fu, Y.F. Li, G.Z. Liu, Effect of orientation and lamellar spacing of Fe_2B on interfaces and corrosion behavior of Fe-B alloy in hot-dip galvanization. Acta Mater. **115**, 392–402 (2016)
10. X.Y. Ren, H.G. Fu, J.D. Xing, Y.W. Yang, S.L. Tang, Effect of boron concentration on microstructures and properties of Fe–B–C alloy steel. J. Mater. Res. **304**, 1–11 (2017)
11. J.J. Zhang, Y.M. Gao, J.D. Xing, S.Q. Ma, D.W. Yi, J.B. Yan, Effects of chromium addition on microstructure and abrasion resistance of Fe–B cast alloy. Tribol. Lett. **44**, 31–39 (2011)
12. Y.L. Yi, Q. Li, J.D. Xing, H.G. Fu, D.W. Yi, Y.Z. Liu, B.C. Zheng, Effects of cooling rate on microstructure, mechanical properties, and residual stress of Fe-2.1B (wt%) alloy. Mater. Sci. Eng. A **754**, 129–139 (2019)
13. H.G. Fu, New development of high boron wear-resistant alloy. Foundry Technol. **55**, 292–295 (2006)
14. J.J. Zhang, X.W. Wei, J. Wang, Q.F. Tang, Research progress of wear resistant Fe-B alloy. Foundry **63**, 669–674 (2014)
15. O. Ozdemir, M. Usta, C. Bindal, A.H. Ucisik, Hard iron boride (Fe_2B) on 99.97 wt% pure iron. Vacuum **80**, 1391–1395 (2006)
16. M.S. Li, X.L. Fu, W.D. Xu, R.L. Zhang, R.H. Yu, Valence electron structure of Fe_2B phase and its eigen-brittleness. Acta Metall. Sin. **31**, 201–208 (1995)
17. Y.X. Jian, Z.F. Huang, J.D. Xing, B.C. Zheng, L. Sun, Y.Z. Liu, Y.M. Liu, Effect of improving Fe2B toughness by chromium addition on the two-body abrasive wear behavior of Fe-3.0 wt% B cast alloy. Tribol. Int. **101**, 331–339 (2016)
18. Y.L. Yi, J.D. Xing, X.Y. Ren, H.G. Fu, Q. Li, D.W. Yi, Investigation on abrasive wear behavior of Fe-B alloys containing various molybdenum contents. Tribol. Int. **135**, 237–245 (2019)
19. C. Zhou, J. Xing, B. Xiao, J. Feng, X. Xie, Y. Chen, First principles study on the structural properties and electronic structure of X2B (X=Cr, Mn, Fe Co, Ni, Mo and W) compounds. Comput. Mater. Sci. **44**, 1056–1064 (2009)
20. B. Xiao, J. Feng, C. Zhou, J. Xing, X. Xie, Y. Cheng, R. Zhou, The elasticity, bond hardness and thermodynamic properties of X2B (X=Cr, Mn, Fe Co, Ni, Mo, W) investigated by DFT theory. Phys. B: Condens. Mater. **405**, 1274–1278 (2010)
21. B. Xiao, J.D. Xing, S.F. Ding, W. Su, Stability, electronic and mechanical properties of Fe_2B. Phys. B: Condens. Mater. **403**, 1723–1730 (2008)
22. S.Q. Ma, W.J. Pan, J.D. Xing, S.Q. Guo, H.G. Fu, P. Lyu, Microstructure and hardening behavior of Al-modified Fe-1.5 wt%B-0.4 wt %C high-speed steel during heat treatment. Mater. Charact. **132**, 1–9 (2017)
23. Y.W. Yang, H.G. Fu, Y.P. Lei, K.M. Wang, L.L. Zhu, L. Jiang, Phase diagram calculation and analyze on cast high-boron high-speed steel. J. Mater. Eng. Perform. **25**, 409–420 (2016)
24. Z. Lv, H.G. Fu, J.D. Xing, S.Q. Ma, Y. Hu, Microstructure and crystallography of borides and mechanical properties of Fe-B-C-Cr-Al alloys. J. Alloy. Compd. **662**, 54–62 (2016)
25. H.G. Fu, Q. Xiao, J.C. Kuang, Z.Q. Jiang, J.D. Xing, Effect of rare earth and titanium additions on the microstructures and

properties of low carbon Fe–B cast steel. Mater. Sci. Eng. A **466**, 160–165 (2007)

26. Y.L. Yi, J.D. Xing, M.J. Wan, L.L. Yu, Y.F. Lu, Y.X. Jian, Effect of Cu on microstructure, crystallography and mechanical properties in Fe-B-C-Cu alloys. Mater. Sci. Eng. A **708**, 274–284 (2017)
27. W.R. Thorpe, B. Chicco, Fe-rich corner of the metastable C-Cr-Fe liquidus surface. Metall. Trans. A **16**, 1541–1549 (1985)
28. Y.H. Liu, Y.Q. Wu, T. Shan, Z.K. Wang, G.C. Jiang, Molecular dynamics simulation of phase transformation of δ-Fe→γ-Fe→liquid in continuos temperature-rise process. Acta. Metall. Sin. **46**, 172–178 (2010)
29. P. Christodoulou, N. Calos, A step towards designing Fe-Cr-B-C cast alloys. Mater. Sci. Eng. A **301**, 103–117 (2001)
30. C.Q. Guo, P.M. Kelly, Modeling of spatial distribution of the eutectic M2B borides in Fe-Cr-B cast irons. J. Mater. Sci. **39**, 1109–1111 (2004)
31. Y.B. Wang, X.Z. Liao, Y.H. Zhao, E.J. Lavernia, S.P. Ringer, Z. Horita, T.G. Langdon, Y.T. Zhu, The role of stacking faults and twin boundaries in grain refinement of a Cu–Zn alloy processed by high-pressure torsion. Mater. Sci. Eng. A **527**, 4959–4966 (2010)
32. Y. Li, Z. Zhang, R. Vogt, J.M. Schoenung, E.J. Lavernia, Boundaries and interfaces in ultrafine grain composites. Acta Mater. **59**, 7206–7218 (2011)
33. H. Attar, S. Ehtemam-Haghighi, D. Kent, I.V. Okulov, H. Wendrock, M. Bonisch, A.S. Volegov, M. Calin, J. Eckert, M.S. Dargusch, Nanoindentation and wear properties of Ti and Ti-TiB composite materials produced by selective laser melting. Mater. Sci. Eng. A **688**, 20–26 (2017)
34. P. Majumdar, S.B. Singh, M. Chakraborty, Elastic modulus of biomedical titanium alloys by nano-indentation and ultrasonic techniques—a comparative study. Mater. Sci. Eng. A **489**, 419–425 (2008)
35. A. Hynowska, E. Pellicer, J. Fornell, S. González, N.V. Steenberge, S. Suriñach, A. Gebert, M. Calin, J. Eckert, M.D. Baró, Substructured β-phase Ti–31.0 Fe–9.0 Sn and sub-μm structured Ti–39.3 Nb–13.3 Zr–10.7 Ta alloys for biomedical applications: microstructure benefits on the mechanical and corrosion performances. Mater. Sci. Eng. C **32**, 2418–2425 (2012)
36. Y.Z. Wang, H.S. Ding, H.Z. Zhang, R.R. Chen, J.J. Guo, H.Z. Fu, Microstructures and fracture toughness of Ti–(43–48) Al–2Cr–2Nb prepared by electromagnetic cold crucible directional solidification. Mater. Des. **64**, 153–159 (2014)
37. X.F. Ding, J.P. Lin, H. Qi, L.Q. Zhang, X.P. Song, G.L. Chen, Microstructure formation in γ–γ′ Co–Al–W–Ti alloys during directional solidification. J. Alloys Compd. **509**, 4041–4046 (2011)
38. T. Liu, L.S. Luo, L. Wang, N.N. Guo, X.Z. Li, R.R. Chen, Y.Q. Su, J.J. Guo, H.Z. Fu, Influence of thermal stabilization treatment on microstructure evolution of the mushy zone and subsequent directional solidification in Ti-43Al-3Si alloy. Mater. Des. **97**, 392–399 (2016)
39. Y. Gu, P. Tian, W. Xu, X.L. Han, B. Liao, F.R. Xiao, Non-isothermal prior austenite grain growth of a high-Nb X100 pipeline steel during a simulated welding heat cycle process. Mater. Des. **89**, 589–596 (2016)
40. W.C. Oliver, G.M. Pharr, An improved technique for determining hardness and elastic modulus using load and displacement sensing indentation experiments. J. Mater. Res. **7**, 1564–1583 (1992)
41. Y.V. Milman, B.A. Galanov, S.I. Chugunova, Plasticity characteristic obtained through hardness measurement. Acta. Metall. et Mater. **41**, 2523–2532 (1993)